Check for updates

RESEARCH ARTICLE

ADVANCED HEALTHCARE MATERIALS
www.advhealthmat.de

Geometric Adjustment of T Cell-Sensitive Nanorobots for Enhanced Stability

Yoojin Lee, Dahae Kim, Taihyun Kim, Chae-Won Moon, Hyungseok Yong, Sung-eun Heo, Bumgyu Choi, Yoogyeong Oh, Woojin Choi, Kyungtae Park, Sang-Jun Ha, and Jinkee Hong**

Personalized dendritic cell (DC) based vaccines offer promising immunotherapeutic approaches for cancers and infectious diseases by leveraging living DCs to stimulate a patient's immune system through interactions with T cells. However, conventional DC-based vaccines face significant challenges, including limited stability and short storage lifespan of the living cells. To overcome these limitations, smart artificial nanorobots, termed nano-bone marrow dendritic cell (BMDC)-originated T cell activators (nano-BOTs) are developed by incorporating 1-dimensional (1D) nanoparticles to enhance stability and activation efficacy. The use of 1D nanoparticles enables precise modulation of the geometric properties, resulting in significantly improved interactions with effector T cells. This innovative approach addresses the inherent limitations of traditional DC-based vaccines and amplifies their ability to activate effector T cells. The advanced nanorobots exhibit exceptional stability and therapeutic potential, representing a transformative step toward personalized DC-based vaccines in future biological therapeutics.

1. Introduction

The tumor microenvironment is highly immunosuppressive, leading to the downregulation of the function and number of immune cells, including T cells, natural killer (NK) cells, B cells, and dendritic cells (DCs). This suppression promotes tolerance to cancer therapies,[1] undermining their efficacy. To address this issue, adoptive cell therapy, an immunotherapy approach that enhances a patient's immune system, has garnered significant attention. Among immune cells, DCs play a pivotal role in adoptive cell therapy,[2–7] bridging innate and adaptive immunity by presenting antigens to stimulate T cells and sustain immune responses.[8] DC-based vaccines counteract the tumor microenvironment's immunosuppressive effects by strengthening the T cell activation signals via MHC class I,[9] CD40,[10] CD80, CD86,[11] and ICAM-1.[12,13] These molecules serve as critical barcodes for T cells, facilitating activation, proliferation, and stable adhesion, thus enabling effective immune responses. As a result, DC-based vaccines have emerged as a crucial tool in cancer immunotherapy.

Effective T cell activation, however, depends on the successful delivery of DCs in a healthy state. Challenges such as low storage stability[14] and the limited quantity of DCs[15] pose significant barriers. For instance, during mononuclear cell separation, DCs represent only 0.1–1% of peripheral blood cells, necessitating enrichment processes. Securing a sufficient quantity of stable DC vaccines is a time-consuming process, and their efficacy remains uncertain even after successful isolation.[16] To overcome these challenges and maintain the T cell activation effects of live DCs, our previous work developed immortal DC-based nanoparticles by grafting bone marrow dendritic cell (BMDC) membranes onto 0-dimensional (0D) nanospheres.[17] These 0D nanoparticles feature a nanoscale size and uniform spherical structure, working as ideal carriers for biomimetic membrane coating.

In nanotherapeutic approaches, the modulation of geometric properties has attracted considerable interest due to its influence on in vivo behavior, including interactions with cells, cellular uptake, biodistribution, and targeting efficiency.[18] While 0D nanomaterials such as nanospheres and nanotubes are popular for drug delivery due to their ease of synthesis, they often suffer from limited targeting efficiency due to their extremely small size.[19] Although nanoparticles larger than 300 nm have

---

Y. Lee, T. Kim, H. Yong, S.-eun Heo, B. Choi, Y. Oh, W. Choi, K. Park, J. Hong
Department of Chemical & Biomolecular Engineering
College of Engineering
Yonsei University
50 Yonsei-ro, Seodaemun-gu, Seoul 03722, Republic of Korea
E-mail: jinkee.hong@yonsei.ac.kr

D. Kim, C.-W. Moon, S.-J. Ha
Department of Biochemistry
College of Life Science & Biotechnology
Yonsei University
50 Yonsei-ro, Seodaemun-gu, Seoul 03722, Republic of Korea
E-mail: sjha@yonsei.ac.kr

The ORCID identification number(s) for the author(s) of this article can be found under https://doi.org/10.1002/adhm.202500846

© 2025 The Author(s). Advanced Healthcare Materials published by Wiley-VCH GmbH. This is an open access article under the terms of the Creative Commons Attribution-NonCommercial-NoDerivs License, which permits use and distribution in any medium, provided the original work is properly cited, the use is non-commercial and no modifications or adaptations are made.

DOI: 10.1002/adhm.202500846

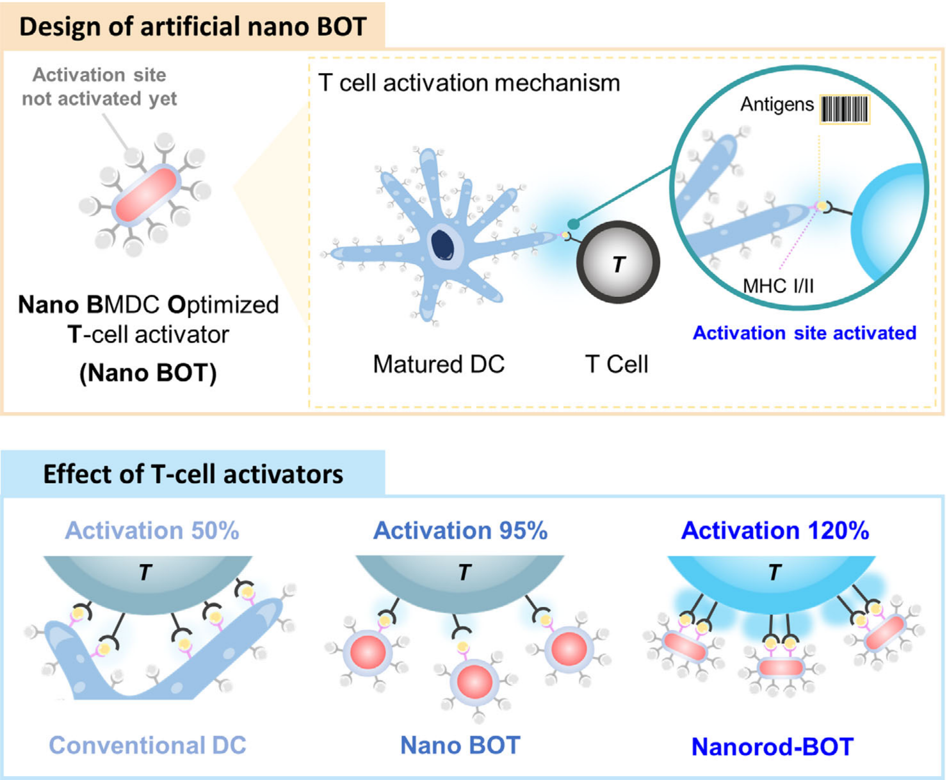

Scheme 1. Schematic illustrations of nano-sized BMDC-originated T cell activators (nano-BOTs). Showcasing optimized activating sites for enhanced living T cell activation.

shown enhanced stimulation of CD8$^+$ T cells,[20] their larger size risks in vivo embolization and reduced biodistribution.[21] In addition to the 0D nanoparticles, various 2-dimensional (2D) nanomaterials such as graphene (oxide), MXene,[22] metal–organic framework (MOF)[23,24] have also been utilized as effective drug delivery systems due to their large surface area, however, 2D materials are known to potentially cause toxicity and immune responses,[25] and they can also be easily phagocytosed and removed by macrophages before reaching the targeting site.[26] In contrast, 1-dimensional (1D) nanomaterials offer several advantages. These materials are non-toxic,[27] capable of evading macrophage phagocytosis,[28,29] and maintain a large surface area for conjugating higher amounts of targeting moieties compared to 0D nanomaterials.[30] Additionally, they overcome the toxicity and immune response issues associated with 2D nanomaterials, which are prone to macrophage clearance before reaching their target sites.

Inspired by DCs' natural ability to present multiple activation sites for efficient antigen presentation,[31] in this study, we designed nano-sized BMDC-originated T cell activators (nano-BOTs) by modulating the geometric properties of nanoparticles (**Scheme** 1). The nano-BOTs remain inactive until they encounter a CD8$^+$ T cell. Upon interaction with the T cell receptor, the nano-BOT autonomously illuminates to activate the CD8$^+$ T cells, resembling a robot that illuminates and operates only in its intended environment. By optimizing the dimensions of nanoparticles, the design not only improves the effectiveness of DC vaccines but also enhances the stability of nano-BOTs, addressing limitations not previously overcome. This innovative approach amplifies activation sites and improves nanoparticle stability, significantly increasing the sensitivity and operational efficiency of nano-BOTs in cancer immunotherapy.

2. Results and Discussion

2.1. Preparation of Nano-BOTs

We designed nano-BOTs capable of generating T cell activation effects. To fabricate the nano-BOTs, phospholipids, and receptors that serve as T cell activators were first isolated and extracted from harvested BMDCs. The BMDCs were then formulated into vesicles with multiple activation sites via ultrasonication (**Figure** 1a). Next, we used nanoparticles (NPs) as carriers to deliver these activation sites. We synthesized original spherical NPs (ONP) and then modulated the length along the x-axis to create elongated NPs (LNP) and shortened NPs (SNP) (Figure 1b). To optimize activation efficiency, the diameter along the y-axis was maintained. The sizes of the synthesized NPs were confirmed by transmission electron microscopy (TEM). The ONP had a diameter of 71.02 ± 10.20 nm, LNPs had a length of 127.85 ± 9.31 nm and a diameter of 69.11 ± 4.96 nm, and SNPs had a length of 59.38 ± 8.32 nm and a diameter of 17.02 ± 2.39 nm (Figure 1d–f; Figures S1 and S2). The surface areas per volume for ONPs, LNPs, and SNPs were calculated to be 0.1,

21922659, 2025, 15, Downloaded from https://advanced.onlinelibrary.wiley.com/doi/10.1002/adhm.202500846 by Yonsei University Library, Wiley Online Library on [06/04/2026]. See the Terms and Conditions (https://onlinelibrary.wiley.com/terms-and-conditions) on Wiley Online Library for rules of use; OA articles are governed by the applicable Creative Commons License

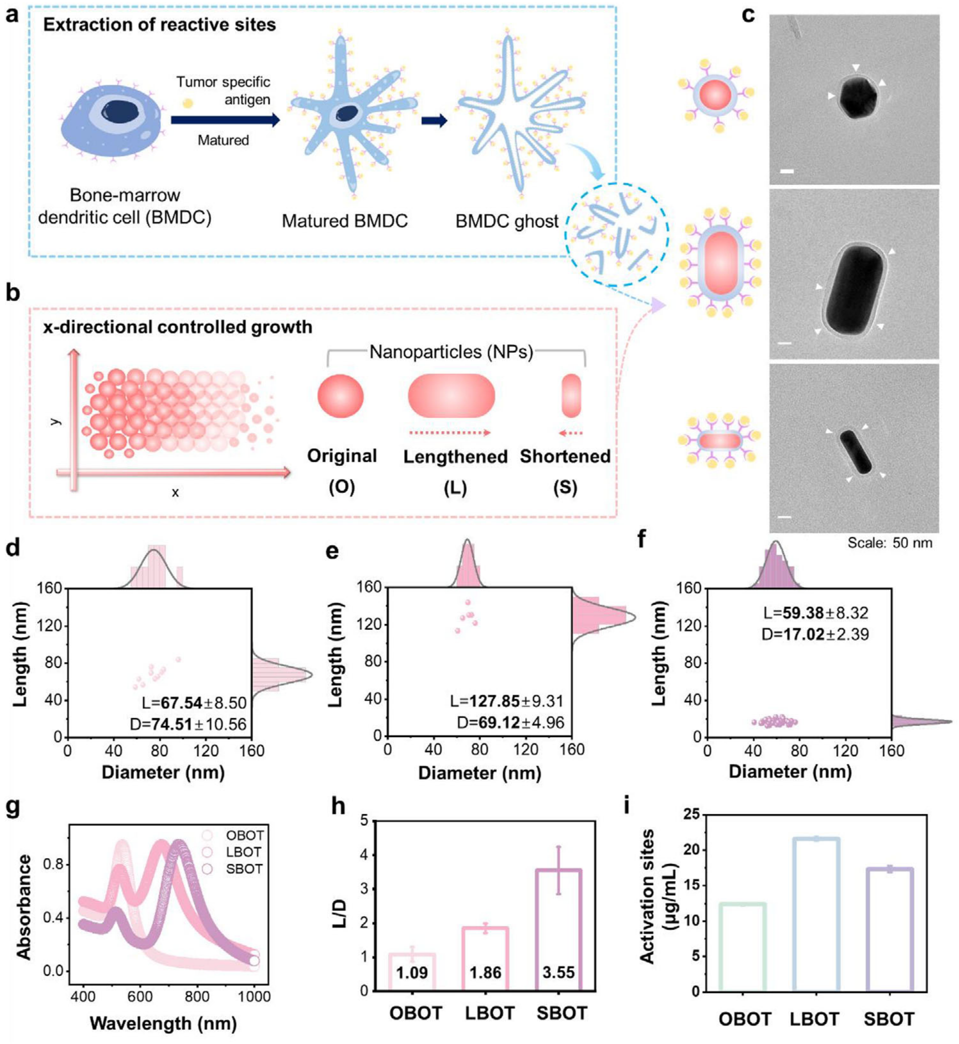

Figure 1. Characterization of nano-BOTs. a) BMDC membranes for T cell activation were isolated from BMDCs. b) Nanoparticles were elongated or shortened along the x-axis from their original spherical form to optimize the nano-BOTs. c) Nano-BOTs were synthesized, and their morphologies were analyzed by TEM. The size distributions of d) ONPs, e) LNPs, and f) SNPs were determined by TEM.
g) Wavelengths were measured by UV–vis spectroscopy to compare the synthesized nanoparticles. h) The L/D ratios of the NPs were calculated using TEM and ImageJ. i) The amount of activation sites on the nanoparticles was quantified.

0.23, and 0.08 nm^2, respectively (Figure S3, Supporting Information). These results indicate that LNPs had the largest surface area, followed by ONPs and SNPs, as the LNPs were elongated from the spherical form. A short wavelength of ≈520 nm corresponds to a length/diameter (L/D) ratio of 1, with the wavelength increasing as the L/D ratio increases.[32] Using ultraviolet-visible (UV-Vis) spectroscopy, we observed a red shift in the longitudinal surface plasmon resonance (LSPR) wavelength redshifted as the L/D increased (Figure 1g; Figure S4, Supporting Information). The L/D ratios of ONPs, LNPs, and SNPs were calculated as 1.09 ± 0.22, 1.86 ± 0.14, and 3.55 ± 0.69, respectively (Figure 1h). In conclusion, we successfully synthesized NPs with distinct characteristics by controlling the length and diameter of the nanoparticles from their original spherical form.

Previous studies have indicated that nanoparticles containing hexadecyltrimethylammonium bromide (CTAB) exhibit cytotoxicity and carry positive charges on their surface.[33,34] In this study, NPs were fabricated using CTAB as a surfactant. Nanoparticles with positive charges are typically coated with an external BMDC membrane, which contains receptors that should be oriented outward due to the strong interaction between the outer membrane of BMDC and the nanoparticles.[35] In contrast, nanoparticles with negative surface charges can be coated with the BMDC membrane in a right-side-out direction. Therefore, we switched the surfactant from CTAB to citrate to introduce a negative charge on the surface, facilitating the right-side-out coating of the BMDC membrane and eliminating cytotoxicity. As a result, all the synthesized NPs were successfully modified to have a negative surface charge (Figure S5, Supporting

© 2025 The Author(s). Advanced Healthcare Materials published by Wiley-VCH GmbH

21922659, 2025, 15, Downloaded from https://advanced.onlinelibrary.wiley.com/doi/10.1002/adhm.202500846 by Yonsei University Library, Wiley Online Library on [06/04/2026]. See the Terms and Conditions (https://onlinelibrary.wiley.com/terms-and-conditions) on Wiley Online Library for rules of use; OA articles are governed by the applicable Creative Commons License

21922659, 2025, 15, Downloaded from https://advanced.onlinelibrary.wiley.com/doi/10.1002/adhm.202500846 by Yonsei University Library, Wiley Online Library on [06/04/2026]. See the Terms and Conditions (https://onlinelibrary.wiley.com/terms-and-conditions) on Wiley Online Library for rules of use; OA articles are governed by the applicable Creative Commons License

Information). Furthermore, there was no observed cytotoxicity against RAW 264.7 macrophage cells (Figure S6, Supporting Information). These findings suggest that the NPs are suitable for BMDC membrane coating due to their biocompatibility and consistent negative charge. Consequently, the as-prepared NPs and the isolated BMDC membranes were sonicated to integrate the BMDC membrane onto the nanoparticles, creating the nano-BOTs (Figure 1c). TEM images revealed a coating thickness of 10–20 nm around the nanoparticle surfaces, confirming that the BMDC membranes were successfully and completely coated on the NPs.

After introducing BMDC membranes onto the surface of NPs, the surface charges of ONPs, LNPs, and SNPs decreased from −67.33 ± 1.68 mV, −86.5 ± 1.4 mV, and −75.85 ± 9.45 mV to −56.13 ± 0.38 mV, −77.15 ± 0.55 mV, and −59.05 ± 0.55 mV, respectively. The zeta potential results indicate that the surface charge values of the nano-BOTs approached those of the BMDC membranes, which had a charge of −55.53 ± 1.11 mV (Figure S7, Supporting Information), confirming the successful formation of nano-BOTs through membrane coating. Additionally, the hydrodynamic sizes of the NPs were measured via dynamic light scattering (DLS) (Figures S8–S10, Supporting Information). To further verify the presence of activation sites from the BMDC membranes on the NPs, we quantified the protein content on the nano-BOT surface using a BCA assay (Figure 1i). OBOTs, LBOTs, and SBOTs showed protein contents of 12.39, 21.59, and 17.34 µg mL^{-1}, respectively, with LBOTs exhibiting the highest protein content and thus the largest number of activation sites. Moreover, to quantify the phospholipids on the nano-BOT surfaces derived from the BMDC membranes, we measured the fluorescence intensity of DiD-stained phospholipids using photoluminescence (PL) spectroscopy (Figure S11, Supporting Information). The results indicated that LBOTs exhibited the highest phospholipid content, consistent with their protein content. This suggests that LBOTs may have a higher number of T cell activation sites on their surface compared to the other nano-BOTs at the same particle concentration, owing to their larger surface area.

2.2. Storage Stability of Nano-BOTs

Activation sites can be cloaked on the surface of nanoparticles using extrusion or bath sonication methods.[36] However, due to differences in NP length and diameter, controlling the coating efficiency during extrusion may be challenging. This is because: 1) particles may become trapped in the pores of the filter membrane in the extruder, or 2) variations in cell membrane coating efficiency may occur, as particles of different sizes could interact differently with the membrane, despite the filter membrane having a uniform pore size. To address these issues, we compared and evaluated the efficiency of BMDC membrane coating on NPs using bath sonication, which facilitated the camouflage of NPs with BMDC membranes. Nano-BOTs were fabricated under identical sonication time and energy conditions for comparative analysis. Typically, phospholipids containing activation sites with high curvature exhibit a fluidic structure, resulting in sparse phospholipid arrangements and high surface tension, which can lead to unstable coatings.[37] In contrast, phospholipids with planar structures tend to form denser coatings due to strong interactions between lipid bilayers, resulting in low surface tension and high coating stability. As the L/D ratio of NPs increases, the proportion of planar structures also increases. Based on this, we hypothesized that SBOTs would exhibit the highest coating stability among all the nano-BOTs (**Figure 2**a). To test this, we stored the nano-BOTs for 1 and 7 days and observed any changes in the stability of the BMDC membrane coating.

TEM analysis revealed that the BMDC membrane coating on OBOTs swelled and ruptured, and a similar phenomenon was observed in LBOTs, particularly along the short axis where curvature was most pronounced. In contrast, SBOTs maintained a dense, intact coating around the nanoparticles, showing no signs of swelling or rupture (Figure 2b). Statistical analysis also revealed that OBOTs swelled ≈2.5 times more than on the first day of coating, LBOTs showed a proportional loss of coating, while SBOTs maintained coating stability (Figure S12, Supporting Information). Next, we measured the hydrodynamic sizes of the nano-BOTs by DLS. The size of OBOTs significantly decreased, suggesting that the BMDC membrane had ruptured and detached from the surface (Figure S13, Supporting Information). Conversely, the size of LBOTs decreased after 7 days of storage (Figure S14, Supporting Information), likely due to swelling of the BMDC membrane, which remained attached to the surface. However, SBOTs did not exhibit any increase or decrease in size (Figure S15, Supporting Information), indicating their high coating stability. Overall, these DLS results suggest that stability increased as the L/D ratio increased, consistent with the TEM observations (Figure 2c).

Additionally, BCA assay results showed that the concentrations of activation sites on OBOTs, LBOTs, and SBOTs retained 53.27%, 70.58%, and 100% of their initial values, respectively (Figure 2d; Figure S16, Supporting Information). Similarly, the amounts of phospholipids retained were 29.19%, 45.45%, and 100% for OBOTs, LBOTs, and SBOTs, respectively (Figure 2e–h). Importantly, flow cytometric analysis using fluorochrome-labeled mAbs against MHC class II, a major surface molecule of DCs, revealed that SBOTs exhibited the highest level of expression (Figure S17, Supporting Information), confirming stable membrane retention on the surface of SBOTs. As predicted, the increase in the L/D ratio enhanced the stability of nano-BOTs by increasing the proportion of planar structures relative to curved ones.

Confirming the long-term stability of SBOT, we additionally determined the stability of nano-BOTs in several conditions such as temperature and pH (**Figure 3**a). Nano-BOTs were stored under three different temperature conditions: 4 °C, the standard storage temperature for pharmaceuticals; 25 °C, representing room temperature; and 37 °C, to simulate physiological conditions during circulation in the body after administration. Furthermore, their storage stability was assessed under both a physiologically neutral pH and an acidic pH, the latter reflecting the tumor microenvironment. The detected PL intensity of phospholipids showed a decrease in coating stability of T cell activators as the temperature increased to 25 and 37 °C in OBOT and LBOT, while SBOT exhibited consistent intensity across all three temperatures (Figure 3b–d). Additionally, BCA assay results indicated a significant reduction in the concentration of T cell activators in OBOT and LBOT with increasing temperature, whereas SBOT main-

© 2025 The Author(s). Advanced Healthcare Materials published by Wiley-VCH GmbH

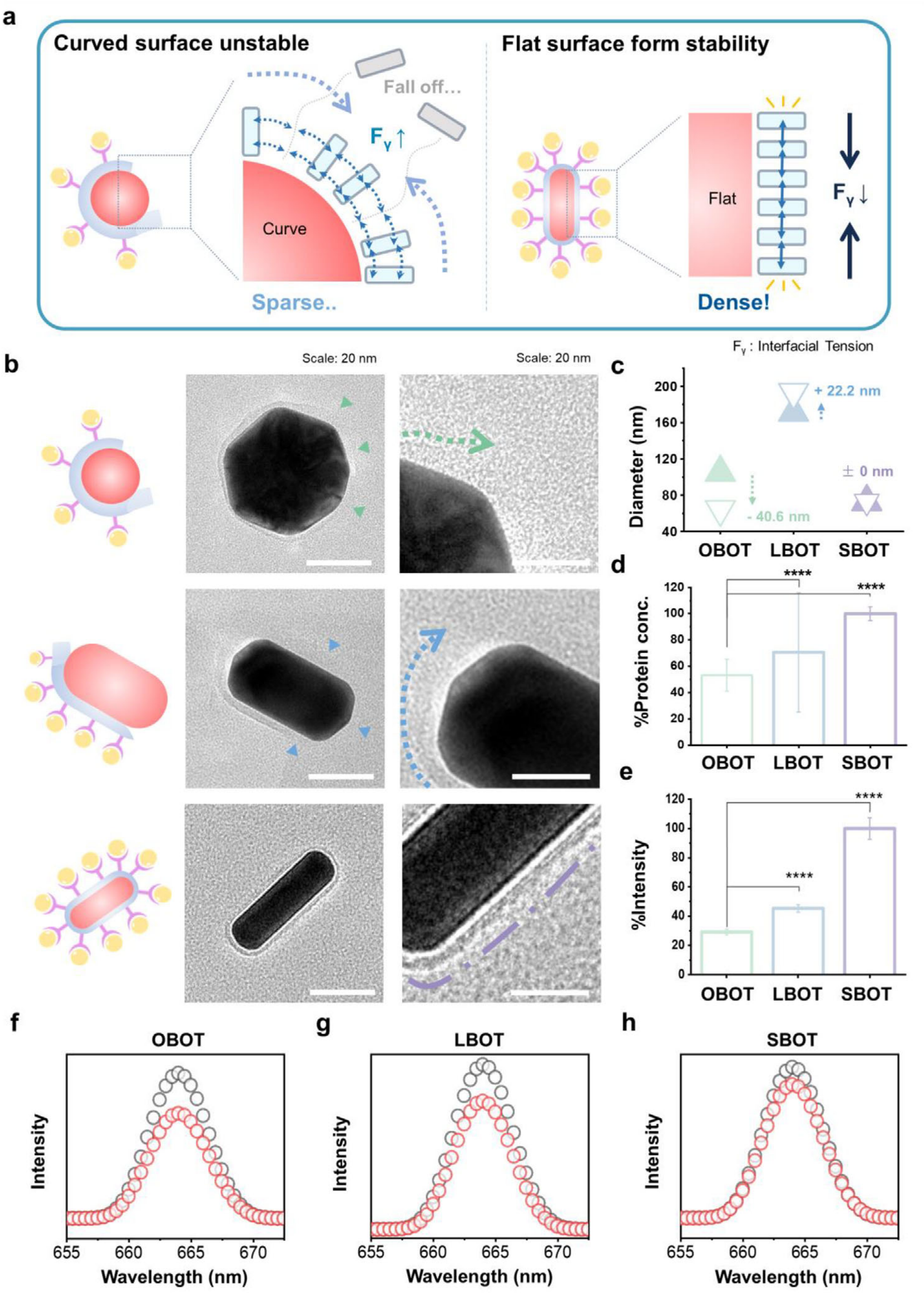

Figure 2. Stability of nano-BOTs after 1 week of storage. a) Magnified illustration of the nano-BOT mechanism based on surface properties. b) TEM images of nano-BOTs on day 7. c) Comparison of sizes after 1 (▲) and 7 (▽) days. d) Protein concentration and e) fluorescence intensity changes after 7 days of storage. f) Changes in PL intensity after 7 days of storage for OBOTs. g) Changes in PL intensity after 7 days of storage for LBOTs. h) Changes in PL intensity after 7 days of storage for SBOTs. Data were analyzed by one-way ANOVA with Tukey's multiple comparison test. The graphs show the mean ±SEM. Data are representative at least two independent experiments ($n = 3$/group). *$p < 0.05$; **$p < 0.01$; ***$p < 0.001$; ****$p < 0.0001$.

tained its stability (Figure 3e). Consistent with the temperature stability results, modulation of pH values to an acidic environment led to a significant reduction in the coating stability of T cell activators in OBOT and LBOT relative to the physiological pH, whereas SBOT exhibited minimal impact (Figure 3f–i). The effects of pH and temperature were further examined by TEM analysis (Figure S18, Supporting Information). In SBOT and LBOT, T cell activators exhibited swelling, while OBOT showed more pronounced swelling, leading to a decrease in phospholipid clarity. Additionally, some rupture was observed in LBOT. In contrast, SBOT maintained the T cell activators across all conditions. Notably, the phospholipid thickness remained similar to

© 2025 The Author(s). Advanced Healthcare Materials published by Wiley-VCH GmbH

21922659, 2025, 15, Downloaded from https://advanced.onlinelibrary.wiley.com/doi/10.1002/adhm.202500846 by Yonsei University Library, Wiley Online Library on [06/04/2026]. See the Terms and Conditions (https://onlinelibrary.wiley.com/terms-and-conditions) on Wiley Online Library for rules of use; OA articles are governed by the applicable Creative Commons License

21922659, 2025, 15, Downloaded from https://advanced.onlinelibrary.wiley.com/doi/10.1002/adhm.202500846 by Yonsei University Library, Wiley Online Library on [06/04/2026]. See the Terms and Conditions (https://onlinelibrary.wiley.com/terms-and-conditions) on Wiley Online Library for rules of use; OA articles are governed by the applicable Creative Commons License

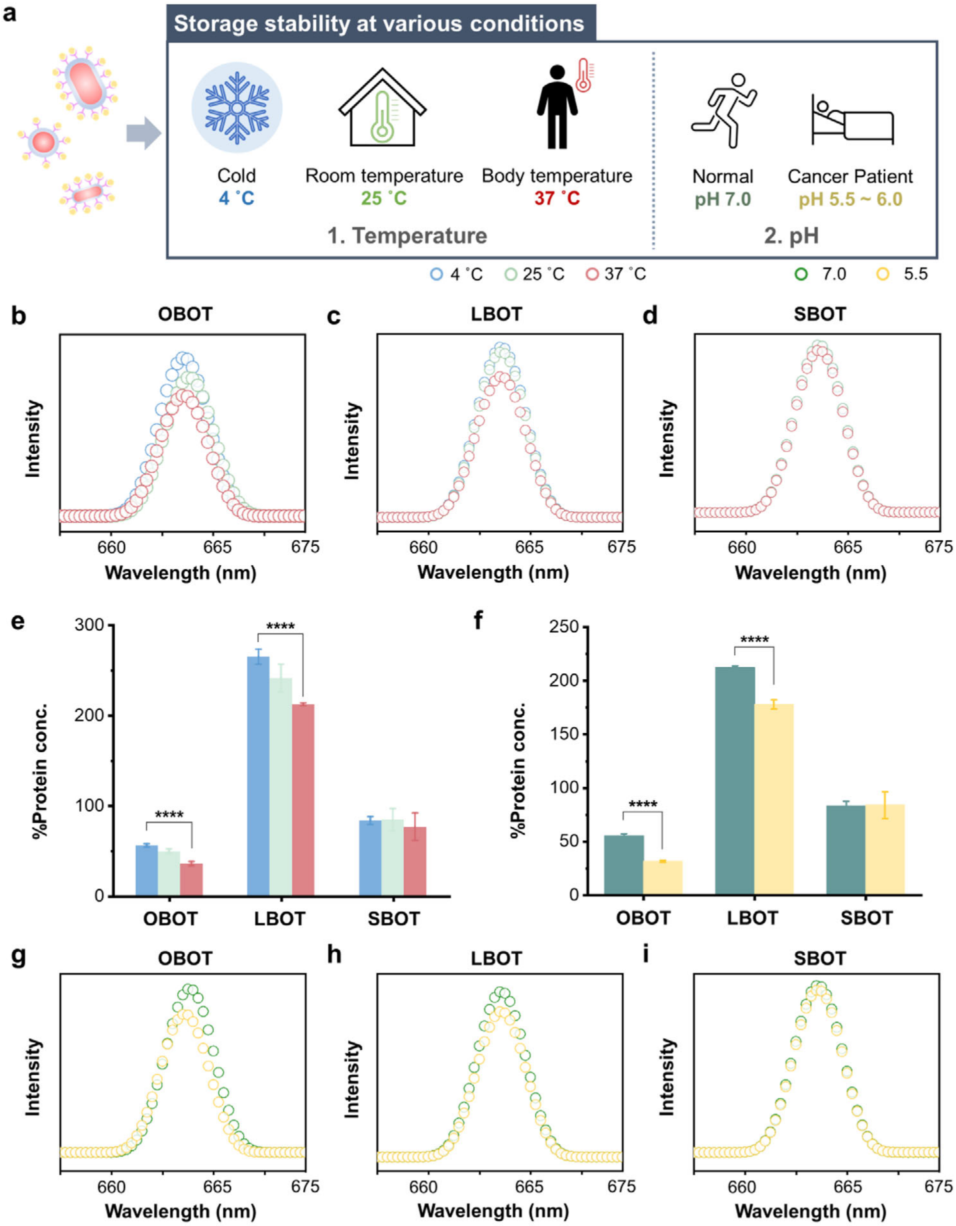

Figure 3. Stability of nano-BOTs with various storage conditions. a) Illustration of the nano-BOT storage condition tests. PL intensity changes under several storage temperature of b) OBOTs, c) LBOTs, and d) SBOTs. Protein concentrations of nano-BOTs under e) different temperatures, and f) pH conditions. Changes in PL intensity of g) OBOTs, h) LBOTs, and i) SBOTs under the physiological (7.0) and acidic pH (5.5) conditions. Data were analyzed by one-way ANOVA with Tukey's multiple comparison test. The graphs show the mean ± SEM. Data are representative at least two independent experiments ($n = 3$/group). *$p < 0.05$; **$p < 0.01$; ***$p < 0.001$; ****$p < 0.0001$.

its original state even at 37 °C (Figure 2c). The DLS results also showed that the coatings of LBOT and SBOT were relatively stable, while OBOT exhibited significant changes in size, particularly at 37 °C (Figure S19, Supporting Information). Particularly, based on these results, it was evident that the impact of temperature in OBOT was more pronounced than that of pH conditions. In conclusion, SBOT demonstrated not only long-term stability but also the ability to maintain integrity under harsh conditions.

2.3. In Vitro Defensive Ability of Nano-BOTs to Evade Phagocytes for Prolonged Circulation

Neutrophils and macrophages are specialized phagocytes responsible for engulfing foreign particles through phagocytosis, a form of cellular uptake.[38] If nano-BOTs are internalized by these phagocytes, their ability to activate T cells could be compromised, as they may fail to reach the lymph nodes where T cells are located. A large surface area facilitates easy recognition and con-

© 2025 The Author(s). Advanced Healthcare Materials published by Wiley-VCH GmbH

21922659, 2025, 15, Downloaded from https://advanced.onlinelibrary.wiley.com/doi/10.1002/adhm.202500846 by Yonsei University Library, Wiley Online Library on [06/04/2026]. See the Terms and Conditions (https://onlinelibrary.wiley.com/terms-and-conditions) on Wiley Online Library for rules of use; OA articles are governed by the applicable Creative Commons License

tact with phagocytes, while a low L/D ratio reduces the bending energy required for phagocytic cell membrane deformation,[39] thus promoting cellular uptake (**Figure** 4a). To evaluate and compare the ability of nano-BOTs to evade phagocytes, we first cocultured NPs and nano-BOTs with phagocytes for 4 h, followed by washing to remove any non-internalized particles. Inductively coupled plasma mass spectrometry (ICP-MS) was used to quantify the internalized particles precisely. The results indicated that nano-BOTs were less readily internalized by phagocytes, likely due to the BMDC membrane on their surface, and the amount of internalized nano-BOTs decreased with increasing L/D ratio. To further visualize and confirm the internalization of nano-BOTs, we stained them with the fluorescent dye DiD and cocultured them with RAW 264.7 macrophage cells (Figure 4b; Figure S20, Supporting Information). Confocal microscopy images revealed the internalization of nano-BOTs, evident by the red fluorescence within the macrophages. Interestingly, SBOTs were barely present within the actin filaments, whereas OBOTs and LBOTs showed multiple red fluorescence signals within the actin filaments which indicates the internalization of nanoparticles toward the macrophage. This can further facilitate the degradation of nanoparticles by lysosomes[40] or deposition of lysosomal compartment in the cytoplasm.[41] Moreover, LBOTs displayed higher fluorescence intensity in the actin filaments compared to OBOTs (Figure 4d), which contrasts with the data in Figure 4c. This discrepancy may be explained by the larger surface area of LBOTs, which is ≈2.5 times that of OBOTs (Figure 1g), resulting in a proportional increase in fluorescence intensity. Overall, these findings suggest that SBOTs actively evade phagocytosis due to their high L/D ratio and may exert their effects once they reach the lymph nodes.

2.4. In Vitro Ability of Nano-BOTs to Activate Antigen-Specific CD8$^+$ T Cells

To verify the attachment of T cell activators to the surface of nano-BOTs, we pulsed the nano-BOT with lymphocytic choriomeningitis virus (LCMV) glycoprotein epitope, GP$_{33\text{-}41}$ peptide and cocultured them with P14 CD8$^+$ T cells, which express T cell receptor (TCR) specific for GP$_{33\text{-}41}$ peptide presented in the context of H-2D^b, for 72 h. This allowed us to evaluate and compare the ability of nano-BOTs to activate antigen-specific CD8$^+$ T cells. Proliferation and activation levels of P14 CD8$^+$ T cells were assessed by tracking the CTV dilution, and the expression of CD44 was analyzed (**Figure** 5a; Figures S21 and S22, Supporting Information). Additionally, we examined the levels of major effector cytokines, including IFN-γ, TNF-α, and IL-2 (Figure 5b).

Peptide-pulsed OBOTs exhibited proliferation levels similar to those of live BMDCs, consistent with our previous study,[17] suggesting that nano-BOTs could serve as a potential alternative to DC vaccines. Notably, SBOTs demonstrated the highest CD44 expression albeit the lowest proliferation velocity, indicating the role of SBOTs in promoting activation rather than proliferation of antigen-specific CD8$^+$ T cells compared to that of LBOTs or OBOTs (Figure 5c,d). Furthermore, SBOTs led to a higher frequency of IFN-γ-producing CD8$^+$ T cells compared to OBOTs and LBOTs, with a slight but significant increase in TNF-α levels, particularly when compared to BMDCs. IL-2 expression was approximately three times higher in LBOTs and two times higher in SBOTs than in OBOTs (Figure 5e). Our experimental data displaying the better functional capacity by SBOTs compared to OBOTs and LBOTs would be mechanistically explained by nanoscale spatial optimization within the immunological synapse. The p-SMAC, a key region of the immunological synapse, is characterized by a dense lateral arrangement of adhesion molecules such as LFA-1 and ICAM-1, which stabilize the synapse and facilitate TCR microcluster movement toward the c-SMAC.[42] Since the p-SMAC spans ≈40 nm in natural immune synapses,[43] the larger surface area of LBOTs may hinder the formation of focused immune synapse clusters. In contrast, SBOTs may promote a more compact and spatially confined interface, facilitating the formation of concentrated immune synapse clusters despite engaging fewer TCRs than LBOTs. Furthermore, as SBOTs exhibited a denser and more tightly adhered membrane coating than OBOTs (Figure 2), it is expected to enhance immune synapse stability and support stronger T cell activation. Our findings suggest that SBOTs may facilitate more focused immune synapse cluster formation, potentially leading to enhanced T cell activation.

Overall, the data indicate that directionally modulated nano-BOTs (especially SBOTs) enhance the activation of antigen-specific CD8$^+$ T cells more effectively than OBOTs (Figures 5f), with SBOTs demonstrating a strong capacity to induce IFN-γ production in effector T cells.

In summary, our results highlight that modulating the directionality of nanoparticles plays a crucial role in T cell activation enhancement, and that nano-BOTs could successfully amplify T cell activation effects compared to live BMDCs, highlighting the potential of nano-BOTs as promising immunotherapeutic agents for amplifying T cell activation, offering the potential for targeting various diseases.

3. Conclusion

Modifying the geometric design of nanomedicines can significantly enhance therapeutic efficacy without the need for extensive chemical modifications or combining them with other therapeutic methods such as chemotherapy. This approach leads to promising, cost-effective immunotherapies with reduced side effects. While DC-based vaccines have shown considerable therapeutic potential, challenges such as limited shelf life, reduced stability, and low production efficiency persist when using live DCs. To overcome these limitations, we extracted the activation sites critical for T cell activation from DCs and incorporated them into 1D nanoparticles. These nanoparticles were designed to enhance the stability of activation sites compared to traditional DC-based vaccines. The fabricated nanorod-shaped BOTs (nano-RodBOTs) demonstrated unique functions, akin to a “robot,” autonomously targeting T cells, delivering barcode-like antigens, and triggering their activation. Additionally, the compact and small SBOTs exhibited significantly better stability than OBOTs and LBOTs, successfully evading immune responses like macrophage uptake, which increased T-cell interactions. Notably, OBOTs, LBOTs, and SBOTs all enhanced T cell activation compared to live DCs. Our work, focused on optimizing T cell activation and extending the half-life of artificial nano cells, presents a superior design strategy and foundational findings that could pave the way for novel ther-

© 2025 The Author(s). Advanced Healthcare Materials published by Wiley-VCH GmbH

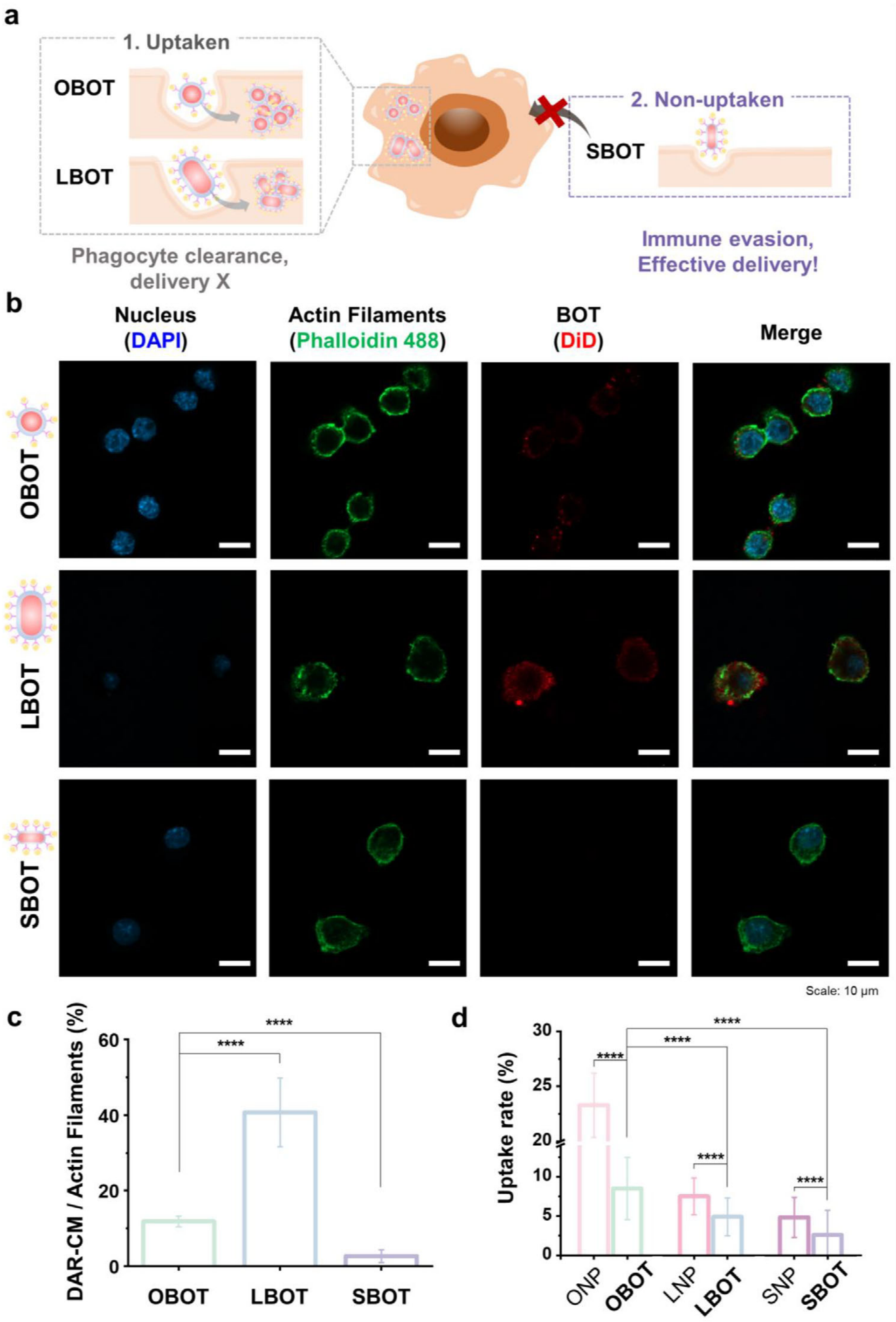

Figure 4. Immune clearance effect analysis results of nano-BOTs. a) Schematic illustration of nano-BOT phagocyte clearance. b) Cellular uptake of NPs and nano-BOTs determined by ICP-MS (mean ± standard deviation (SD), $n = 3$). c) Cellular uptake observed by confocal imaging. d) Mean fluorescence intensity in a single cell (BOT/actin filaments) for nano-BOTs. Data were analyzed by one-way ANOVA with Tukey's multiple comparison test. The graphs show the mean ±SEM. Data are representative at least two independent experiments ($n = 3$/group). $^{*}p < 0.05$; $^{**}p < 0.01$; $^{***}p < 0.001$; $^{****}p < 0.0001$.

21922659, 2025, 15, Downloaded from https://advanced.onlinelibrary.wiley.com/doi/10.1002/adhm.202500846 by Yonsei University Library, Wiley Online Library on [06/04/2026]. See the Terms and Conditions (https://onlinelibrary.wiley.com/terms-and-conditions) on Wiley Online Library for rules of use; OA articles are governed by the applicable Creative Commons License

© 2025 The Author(s). Advanced Healthcare Materials published by Wiley-VCH GmbH

21922659, 2025, 15, Downloaded from https://advanced.onlinelibrary.wiley.com/doi/10.1002/adhm.202500846 by Yonsei University Library, Wiley Online Library on [06/04/2026]. See the Terms and Conditions (https://onlinelibrary.wiley.com/terms-and-conditions) on Wiley Online Library for rules of use; OA articles are governed by the applicable Creative Commons License

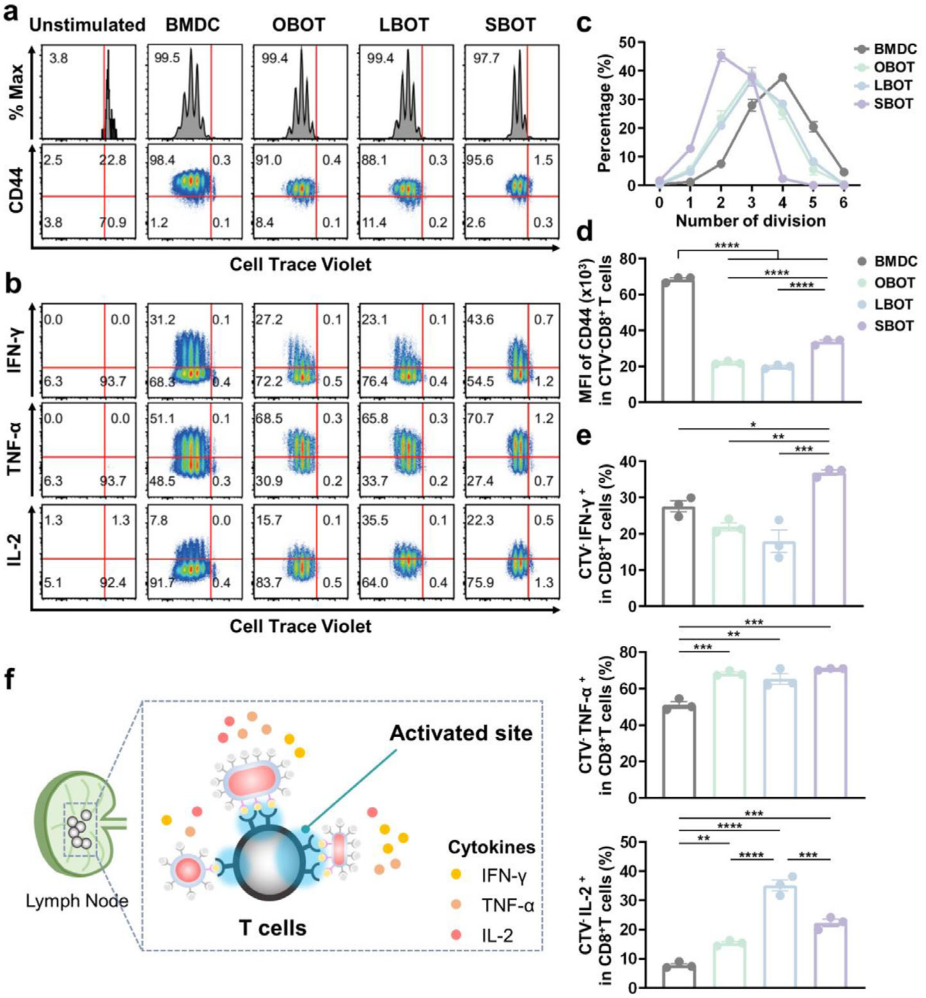

Figure 5. In vitro P14 CD8$^+$ T cell activation analysis of nano-BOTs. a) Flow cytometry data showing P14 CD8$^+$ T cell proliferation (CTV$^-$) assessed by the CTV dilution assay. b) Flow cytometry data demonstrating the cytokine levels of IFN-γ, TNF-α, and IL-2. c) Quantification of cell division using CTV dilution assay. d) MFI of CD44 expression in CTV$^-$ P14 CD8$^+$ T cells. e) The frequencies of CTV$^-$IFN-γ^+, CTV$^-$TNF-α^+, and CTV$^-$IL-2$^+$ in P14 CD8$^+$ T cells. f) Schematic illustration of P14 CD8$^+$ T cells activation by nano-BOTs. Data were analyzed by one-way ANOVA with Tukey's multiple comparison test. The graphs show the mean ± SEM. Data are representative at least two independent experiments ($n = 3$/group). $^*p < 0.05$; $^{**}p < 0.01$; $^{***}p < 0.001$; $^{****}p < 0.0001$.

apeutic approaches. The precise control over nanoparticle shape and surface properties ensures more efficient immune engagement with fewer side effects.

4. Experimental Section

Materials and Reagents: All chemicals used were of analytical grade and commercially available. Ultrapure water obtained from the Milli-Q system was used for all experiments. The following chemicals were purchased from Sigma–Aldrich: hexadecyltrimethylammonium bromide (CTAB, >98.0%), sodium oleate (NaOL, >97.0%), hydrogen tetrachloroaurate trihydrate ($HAuCl_4 \cdot 3H_2O$), L-ascorbic acid (BioUltra, ≥99.5%), silver nitrate ($AgNO_3$, >99%), sodium borohydride ($NaBH_4$, 99%), poly(sodium 4-styrenesulfonate) (average Mw ~70000), and sodium citrate tribasic dihydrate (BioUltra, for molecular biology) were purchased from Sigma-Aldrich.

Synthesis of Nanoparticles: Gold nanoparticles with an L/D ratio of 1 (60 nm diameter, OD 1, stabilized suspension in citrate buffer) were purchased from Sigma-Aldrich. Gold nanorods with a higher L/D ratio were synthesized using a seed-mediated method and a surfactant mixture of CTAB and NaOL as previously described.[44] The seed solution for nanoparticles was prepared by mixing 5 mL of aqueous $HAuCl_4$ (0.5 mᴍ) with 5 mL of CTAB (0.2 ᴍ), followed by the addition of 0.6 mL of fresh $NaBH_4$ (0.01 ᴍ), which was then diluted to 1 mL with cold water. The diluted $NaBH_4$ solution was injected into the seed solution with vigorous stirring at 1200 rpm for 2 min until the solution changed color from yellow to brownish-yellow. The seed solution was then aged at room temperature for 30 min.

For the growth solution preparation, varying amounts of CTAB, NaOL, $AgNO_3$, $HAuCl_4$, HCl, and ascorbic acid were used (Table S1, Supporting Information). CTAB and NaOL were dissolved in 50 mL of water at 50 °C. After cooling the solution to 30 °C, 4 mᴍ $AgNO_3$ was added, and the mixture was allowed to sit undisturbed at 30 °C for 15 min. Then, 50 mL of 1 mᴍ $HAuCl_4$ was added, and the solution was stirred at 700 rpm for 1 h

© 2025 The Author(s). Advanced Healthcare Materials published by Wiley-VCH GmbH

until it became colorless. The pH of the solution was adjusted using 12.1 м (37 wt.%) HCl. After stirring at 400 rpm for 15 min, 0.064 м ascorbic acid was added, and the mixture was stirred vigorously for 30 s. Finally, the seed solution was injected into the growth solution, and the mixture was stirred for 30 s before being left undisturbed at 30 °C for 12 h. The nanoparticles were then isolated by centrifugation at 13 000 rpm for 30 min.

To eliminate the cytotoxic effects of nanoparticles, they were citrate-coated as described in reference.[45] The nanoparticles fabricated with CTAB were washed with deionized water and incubated in a 0.15 wt.% solution of poly(sodium 4-styrenesulfonate) (Na-PSS, MW ≈70 kDa) for 1 h to allow surfactant exchange from CTAB to PSS. This process was repeated three times. The nanoparticles were then resuspended in a 5 mм sodium citrate solution and incubated for 12 h to allow further exchange of PSS with citrate. The excess citrate and PSS were removed by centrifugation with deionized water for three cycles, and the concentration of nanoparticles was measured by inductively coupled plasma-mass spectrometry (ICP-MS, 7900, Agilent, USA). Finally, the concentration of nanoparticles was converted to particle numbers for subsequent experiments.

Characterization of Nanoparticles: The shape and size (length and diameter) of the nanoparticles were visualized and measured using scanning transmission electron microscopy (Cs-TEM, JEM-ARM-200F (NEOARM), JEOL). The average particle size was calculated using ImageJ software. The different L/D ratios were determined by measuring absorbance at specific wavelengths using ultraviolet-visible (UV–vis) spectroscopy (Evolution 300, Thermo Fisher, CA, USA).

Mice: Six- to eight-week-old specific pathogen-free female C57BL/6 (B6) mice were purchased from Orient Bio. LCMV GP33-41 epitope-specific T cell receptor transgenic P14 mice were provided by Dr. Rafi Ahmed (Emory University, School of Medicine, Atlanta, GA, USA). All experiments were conducted with the approval of the International Animal Care and Use Committee at Yonsei University, following the Laboratory Animal Act of the Korean Ministry of Food and Drug Safety. This act aims to improve the ethics and reliability of animal testing by ensuring the appropriate administration of laboratory animals and testing (Permit No. IACUC-A-202210-1552-02).

BMDC Differentiation and BMDC Membrane Derivation: BMDCs were differentiated from bone marrow cells isolated from the femurs of naïve C57BL/6 and BALB/c mice (6–8 weeks old). Red blood cells (RBCs) from the bone marrow were lysed using ACK lysis buffer (Gibco Laboratories). After RBC lysis, the resulting single-cell suspensions were cultured in RPMI medium (Corning) supplemented with 10% fetal bovine serum (FBS; Thermo Fisher Scientific), 1% penicillin/streptomycin (P/S) (Thermo Fisher Scientific), and 20 ng mL^{-1} recombinant murine GM-CSF (JW Creagene). The culture media were replenished on days 3 and 6. To mature the BMDCs, 20 ng mL^{-1} LPS (Sigma Aldrich) was added to the culture medium for the final 6 days. Seven days post-culture, nonadherent cells were collected and pelleted by centrifugation at 2000 rpm for 5 min at room temperature. The BMDCs were then resuspended in 1× PBS (pH 7.4) containing an EDTA-free Pierce protease inhibitor mini tablet (PIT) (Sigma Aldrich, 1 tablet per 10 mL of solution).

The BMDC membranes were derived from 1 mL aliquots of BMDC solutions containing $1–2 \times 10^6$ cells through three freeze (−70 °C)–thaw (room temperature) cycles, which facilitated membrane disruption. The aliquots were pelleted by centrifugation at 6000 rpm for 5 min and washed three times with 1× PBS containing PIT to obtain pure cell membranes. The pelleted BMDC membranes were resuspended in 1× PBS and sonicated at 20% amplitude for 60 cycles (3 s of sonication, followed by 2-s intervals on ice) using an ultrasonic processor (VC-505, Sonics & Materials) for a total of 3 min in a capped glass vial.

Preparation of Nano-BOT: BMDC membrane vesicles were added to three different nanoparticles preparations, each mixed at appropriate ratios based on particle number and surface area of nanoparticles and BMDCs. The mixed BMDC membrane vesicles and nanoparticles were sonicated in a water bath for 3 min (150 W). Uncoated BMDC membrane fragments and vesicles were removed by centrifugation, and the nano-BOT nanoparticles were stored at 4 °C in deionized water for characterization, as well as in growth media for cell culture with RAW 264.7 cells and CD8$^+$ T cells.

Peptide Pulsing for CD8$^+$ T Cell Activation: For peptide pulsing, BMDCs and nano-BOT were incubated with the MHC class I-restricted peptide GP33–41 (0.2 μg mL^{-1}), an H-2Db-restricted dominant CD8$^+$ T cell epitope of lymphocytic choriomeningitis virus (LCMV), for 30 min at 37 °C in RPMI supplemented with 10% FBS. After incubation, the peptide-pulsed cells were washed and used for subsequent experiments.

Characterization and Stability of Nano-BOT: The surface morphology of nano-BOT was analyzed via TEM on days 1 and 7 of fabrication. The surface zeta potential of nanoparticles before and after citation, as well as that of nano-BOT, and the hydrodynamic size of nano-BOT, was determined using dynamic light scattering (DLS, SZ-100, Horiba). The total protein content of DC ghosts and nano-BOT was quantified using a BCA protein assay kit (Thermo Fisher Scientific). DiD (Thermo Fisher Scientific) was used to stain the BMDC membranes for 30 min, then coated onto the surface of nanoparticles. The fluorescence intensity was quantified using photoluminescence spectroscopy (FP-8300, JASCO, Tokyo, Japan). The changes in diameter, protein content, and fluorescence intensity were calculated by comparing the nanoparticles on day 7 to day 1. In addition, nano-BOTs were stored at different temperature (4, 25, and 37 °C) and pH (5.5, and 7.0) conditions for 7 days to determine the changes in morphology (TEM), diameter (DLS), protein contents (BCA Assay), and phospholipid contents (PL).

RAW 264.7 Cell Culture, Cytotoxicity, and Cellular Uptake Analysis: RAW 264.7 mouse macrophage cells were obtained from the Korean Cell Line Bank (Seoul, Korea). The cells were cultured in low-glucose Dulbecco's modified Eagle medium (Gibco, Grand Island, NY), supplemented with 10% heat-inactivated fetal bovine serum (Welgene, Gyeongsan, Korea) and 1% penicillin-streptomycin-glutamine (Gibco).

For the cell viability test of nanoparticles after citation, 5×10^4 cells were seeded per well in 24-well plates and treated with samples for 24 h. After treatment, the cells were washed with PBS. A cell counting kit-8 (CCK-8) reagent (Dongin Biotech Co., Korea) was added to the culture medium, and the cells were incubated for 1 h. Absorbance at 450 nm was measured using a plate reader (Spectra Max 340 PC; Molecular Devices, San Jose, CA, USA).

To measure the cellular uptake of nanoparticles, the cells were seeded in 12-well plates and treated with nanoparticles for 4 h. After incubation, the cells were washed with PBS and collected in deionized water. The amount of gold ions internalized by RAW 264.7 cells was measured by ICP-MS. To visualize the cellular uptake of nanoparticles, the particles were stained with DiD, and the cells were seeded in confocal dishes (glass-bottom dishes; SPL Life Science, Pocheon, Korea). The cells were treated with nano-BOTs and incubated for 4 h. After incubation, the cells were washed with PBS and stained with Alexa Fluor 488 phalloidin and DAPI. The intracellular uptake of the particles was observed using confocal microscopy (LSM 980, Carl Zeiss, Oberkochen, Germany). The amount of nano-BOT in a single RAW 264.7 cell was quantified based on intensity using ImageJ software.

CD8$^+$ T Cell Purification and In vitro Coculture Assays: CD8$^+$ T were enriched from the spleens of wild-type P14 mice using the MagniSort Mouse CD8$^+$ T Cell Enrichment Kit (Thermo Fisher Scientific). P14 CD8$^+$ T cells were labeled with 2.5 μм CTV (Life Technologies) for 30 min at 37 °C and washed with RPMI containing 10% FBS. A total of 5×10^4 labeled T cells were cocultured in RPMI containing 10% FBS with 1×10^4 BMDCs and nano-BOT. After 72 h, the cells were harvested, stained, and analyzed by flow cytometry. The co-localization of nano-BOTs and T cells was visualized using confocal microscopy (Carl Zeiss). After 72 h of coculture with DiD-stained nano-BOTs and P14 CD8$^+$ T cells, unbound nano-BOTs were removed by centrifugation at 2500 rpm for 2 min. P14 CD8$^+$ T cells were stained with DAPI (Sigma Aldrich) and FITC-labeled anti-CD8 (BD Biosciences) for 45 min after blocking, followed by visualization.

Antibodies and Flow Cytometry Analysis: For the analysis of lymphocytes, cells were plated in 96-well plates (round bottom) in PBS supplemented with 2% FBS and stained with fluorochrome-conjugated antibodies for 20 min at 4 °C. Fluorochrome-conjugated antibodies against IFN-γ (XMG1.2) and IL-2 (JES6-5H4) were obtained from BD Biosciences; antibodies against CD8 (53-6.7), CD44 (IM7), and MHC II (M5/114/15/2) were obtained from Thermo Fisher Scientific. The antibodies against PD-

© 2025 The Author(s). Advanced Healthcare Materials published by Wiley-VCH GmbH

21922659, 2025, 15, Downloaded from https://advanced.onlinelibrary.wiley.com/doi/10.1002/adhm.202500846 by Yonsei University Library, Wiley Online Library on [06/04/2026]. See the Terms and Conditions (https://onlinelibrary.wiley.com/terms-and-conditions) on Wiley Online Library for rules of use; OA articles are governed by the applicable Creative Commons License

1 (29F.1A12) and TNF-α (MP6-XT22) were obtained from Biolegend. For intracellular staining, antibodies against IFN-γ (XMG1.2), TNF-α (MP6-XT22), and IL-2 (JES6-5H4) were used in combination with anti-CD8 antibodies. Dead cell populations were removed using a Live/Dead fixable stain kit (Thermo Fisher Scientific).

To detect intracellular cytokines in T cells, cells were incubated with the GP33-41 peptide. For GP33-41 T cell stimulation, T cells were restimulated with GP33-41 (0.2 µg mL^{-1}) for 6 h in the presence of Golgi plug/Golgi Stop (BD Biosciences). Peptide was synthesized using the Genscript software. Intracellular Staining was performed after surface staining using the BD Cytofix/Cytoperm fixation/permeabilization kit (BD Biosciences) according to the manufacturer's instructions.

For characterization of antibody (MHCII) on nano-BOTs, the nano-BOTs were stained according to the manufacturer's protocol, and flow cytometry was performed as described previously. Owing to the nanometer scale of anDCs, the anDCs could aggregate more than 2–3 particles together during the staining process. After the measurement, the aggregated anDCs (size>300 nm) were detected and gated to check the antibody levels.

Quantification and Statistical Analysis: All stained samples were analyzed on a CytoFLEX LX (Beckman Coulter) using FlowJo software (Tree Star). Statistical analysis was performed using Origin 2018 and Prism software version 7.0 (GraphPad). Comparisons between multiple groups were performed using one-way ANOVA with Tukey's post hoc test. Statistical details, including the statistical test, the exact value of *n*, precision measure, and statistical significance, are reported in the figures and figure legends.

Supporting Information

Supporting Information is available from the Wiley Online Library or from the author.

Acknowledgements

This work was supported by the National Research Foundation of Korea (NRF) grant funded by the Korean government (MSIP) (RS-2024-00392705). This research was also supported by the National Research Foundation of Korea (NRF) grant (RS-2024-00354178). This work was supported by the Korea US Collaborative Research Fund (RS-2024-00468036). This research was also supported by a grant of the Korea Health Technology R&D Project through the Korea Health Industry Development Institute (KHIDI), funded by the Ministry of Health & Welfare, Republic of Korea (grant number: RS-2024-00437312).

Conflict of Interest

The authors declare no conflict of interest.

Author Contributions

Y.L. and D.K. contributed equally to this work. Y.L. conceptualized the study, conducted the investigation, and wrote the original draft. D.K. conducted the investigation and developed the methodology. T.K. handled visualization and performed validation. C.-W.M. contributed to visualization. S.-e.H. worked on visualization. H.Y. performed validation. B.C. curated the data and developed the software. Y.O. contributed to visualization. W.C. performed validation. K.P. carried out validation. S.-J.H. administered the project, supervised the work, and reviewed and edited the manuscript. J.H. administered the project, supervised the work, and reviewed and edited the manuscript.

Data Availability Statement

The data that support the findings of this study are available from the corresponding author upon reasonable request.

Keywords

dendritic cell, immortalized artificial nanorobots, immune clearance, storage stability, T cell activation

Received: February 15, 2025
Revised: April 16, 2025
Published online: May 8, 2025

---

[1] H. Phuengkham, L. Ren, *Adv. Mater.* **2019**, *31*, 1803322.
[2] M. E. Dudley, S. A. Rosenberg, *Nat. Rev. Cancer* **2003**, *3*, 666.
[3] T. J. Laskowski, A. Biederstädt, K. Rezvani, *Nat. Rev. Cancer* **2022**, *22*, 557.
[4] J. G O'Leary, M. Goodarzi, D. L Drayton, U. H. Andrian, *Nat. Immunol.* **2006**, *7*, 507.
[5] K. F. Bol, G. Schreibelt, M. Bloemendal, W. W. v. Willigen, S. H. Bree, A. L. d. Goede, A. J. d. Boer, K. J. H. Bos, T. D. Boer, M. A. M. O. Nordkamp, T. G. M. v. Oorschot, C. J. Popelier, J. M. Pots, N. M. Scharenborg, M. W. M. M. v. d. Rakt, V. d. Ruiter, W. S. v. Meeteren, M. M. v. Rossum, S. J. Croockewit, B. J. Koeneman, J. H. A. Creemers, I. M. N. Wortel, C. Angerer, M. Brüning, K. Petry, A. Dzionek, A. A. v. d. Veldt, D. J. v. Grünhagen, J. E. M. Werner, J. J. Bonenkamp, et al., *Nat. Commun.* **2024**, *15*, 1632.
[6] A. Mullard, *Nat. Rev. Drug Discovery* **2017**, *16*, 669.
[7] A. Cifuentes-Rius, A. Desai, D. Yuen, A. P. R. Johnston, N. H. Voelcker, *Nat. Nanotechnol.* **2021**, *16*, 37.
[8] P. W. Kantoff, C. S. Higano, N. D. Shore, E. Berger, E. J. Small, D. F. Penson, C. H. Redfern, A. C. Ferrari, R. Dreicer, R. B. Sims, Y. Xu, M. W. Frohlich, P. F. Schellhammer, *N. Engl. J. Med.* **2010**, *363*, 411.
[9] T. Di Pucchio, B. Chatterjee, A. Smed-Sörensen, S. Clayton, A. Palazzo, M. Montes, Y. Xue, I. Mellman, J. Banchereau, J. E Connolly, *Nat. Immunol.* **2008**, *9*, 551.
[10] T. Kikuchi, S. Worgall, R. Singh, M. A. Moore, R. G. Crystal, *Nat. Med.* **2000**, *6*, 1154.
[11] S. Dilioglou, J. M. Cruse, R. E. Lewis, *Exp. Mol. Pathol.* **2003**, *75*, 217.
[12] T. L Flach, G. Ng, A. Hari, M. D Desrosiers, P. Zhang, S. M Ward, M. E Seamone, A. Vilaysane, A. D Mucsi, Y. Fong, E. Prenner, C. C. Ling, J. Tschopp, D. A Muruve, M. W Amrein, Y. Shi, *Nat. Med.* **2011**, *17*, 479.
[13] A. C. I. Steen, M. L. B Grönloh, S. Joosten, F. v. Alphen, M. v. d. Biggelaar, M. A Nolte, M. Spaargaren, J. D. Buul, R. Schoppmeyer, *J. Immunol.* **2023**, *211*, 377.
[14] Z. Sun, J. Liu, Y. Li, X. Lin, Y. Chu, W. Wang, S. Huang, W. Li, J. Peng, C. Liu, *Adv. Mater.* **2023**, *35*, 2208555.
[15] N. Shang, M. Figini, J. Shangguan, B. Wang, C. Sun, L. Pan, Q. Ma, Z. Zhang, *Am. J. Cancer Res.* **2017**, *7*, 2091.
[16] I. A. E. van der Hoorn, G. Flórez-Grau, M. M. van den Heuvel, I. J. M. de Vries, B. Piet, *Front. Immunol.* **2021**, *12*, 704776.
[17] D. Choi, T. G. Kang, T. Kim, C. Moon, M. Choi, D. Kim, T. Kim, Y. Oh, S. Jung, Y. Lee, S. Lee, J. Hong, S.-J. Ha, *Nanotoday* **2024**, *56*, 102237.
[18] P. Guo, D. Liu, K. Subramanyam, B. Wang, J. Yang, J. Huang, D. T. Auguste, M. A. Moses, *Nat. Commun.* **2018**, *9*, 130.
[19] K. R. Rhodes, J. J. Green, *Mol. Immunol.* **2018**, *98*, 13.
[20] J. W. Hickey, F. P. Vicente, G. P. Howard, H. Mao, O. P. Schneck, *Nano Lett.* **2017**, *17*, 7045.
[21] R. Singh, J. W. Lillard Jr., *Exp. Mol. Pathol.* **2009**, *86*, 215.
[22] J. Liu, L. Cui, D. Losic, *Acta Biomater.* **2013**, *9*, 9243.
[23] X. Han, J. Huang, H. Lin, Z. Wang, P. Li, Y. Chen, *Adv. Healthcare Mater.* **2018**, *7*, 1701394.
[24] M. Wu, Y. Yang, *Adv. Mater.* **2017**, *29*, 1606134.
[25] G. A. Naikoo, F. Arshad, M. Almas, I. U. Hassan, M. Z. Pedram, A. A. A. Aljabali, V. Mishra, Á. Serrano-Aroca, M. Birkett, N. B. Charbe, R.

© 2025 The Author(s). Advanced Healthcare Materials published by Wiley-VCH GmbH

21922659, 2025, 15, Downloaded from https://advanced.onlinelibrary.wiley.com/doi/10.1002/adhm.202500846 by Yonsei University Library, Wiley Online Library on [06/04/2026]. See the Terms and Conditions (https://onlinelibrary.wiley.com/terms-and-conditions) on Wiley Online Library for rules of use; OA articles are governed by the applicable Creative Commons License

Goyal, P. Negi, M. El-Tanani, M. M. Tambuwala, *Chem.-Biol. Interact.* **2022**, *365*, 110081.
[26] H. Lin, Z. Song, A. Bianco, *J. Environ. Sci. Health B.* **2021**, *56*, 333.
[27] B. M. Popescu, N. Ali, G. Basturea, G. I. Comsa, L. A. Materon, M. Chipara, *Appl. Surf. Sci.* **2013**, *275*, 2.
[28] J. A. Champion, S. Mitragotri, *Pharm. Res.* **2009**, *26*, 244.
[29] E. Blanco, H. Shen, M. Ferrari, *Nat. Biotechnol.* **2015**, *33*, 941.
[30] R. A. Meyer, J. C. Sunshine, K. Perica, A. K. Kosmides, K. Aje, J. P. Schneck, J. J. Green, *Small* **2015**, *11*, 1519.
[31] R. L Lindquist, G. Shakhar, D. Dudziak, H. Wardemann, T. Eisenreich, M. L Dustin, M. C Nussenzweig, *Nat. Immunol.* **2004**, *5*, 1243.
[32] R. Kumar, L. Binetti, T. Hien Nguyen, L. S. M. Alwis, A. Agrawal, T. Sun, K. T. V. Grattan, *Sci. Rep.* **2019**, *9*, 17469.
[33] A. M. Alkilany, P. K. Nagaria, C. R. Hexel, T. J. Shaw, C. J. Murphy, M. D. Wyatt, *Small* **2009**, *5*, 701.
[34] L. Wang, X. Jiang, Y. Ji, R. Bai, Y. Zhao, X. Wu, C. Chen, *Nanoscale* **2013**, *5*, 8384.
[35] R. H. Fang, A. V. Kroll, W. Gao, L. Zhang, *Cell Membrane Coating Nanotechnol.* **2018**, *30*, 1706759.
[36] L. Liu, D. Pan, S. Chen, M. Martikainen, A. Kårlund, J. Ke, H. Pulkkinen, H. Ruhanen, M. Roponen, R. Käkelä, W. Xu, J. Wang, *Nat. Commun.* **2022**, *13*, 6181.
[37] P. V. Escribá, A. Ozaita, C. Ribas, A. Miralles, E. Fodor, T. Farkas, J. A. García-Sevilla, *Proc. Natl. Acad. Sci. USA* **1997**, *94*, 11375.
[38] P. L. Yèagle, *FASEB J.* **1989**, *3*, 1833.
[39] R. Vácha, F. J. Martinez-Veracoechea, D. Frenkel, *Nano Lett.* **2011**, *11*, 5391.
[40] B. Rathore, K. Sunwoo, P. Jangili, J. Kim, J. H. Kim, M. Huang, J. Xiong, A. Sharma, Z. Yang, J. Qu, J. S. Kim, *Biomaterials* **2019**, *211*, 25.
[41] D. Lee, J. H. Hong, *Pharmaceutics* **2020**, *12*, 217.
[42] M. Dustin, D. Depoil, *Nat. Rev. Immunol.* **2011**, *11*, 672.
[43] J. T Groves, *Curr. Opin. Chem. Biol.* **2006**, *10*, 544.
[44] Y. Du, M. Han, K. Cao, Q. Li, J. Pang, L. Dou, S. Liu, Z. Shi, F. Yan, *ACS Nano* **2021**, *15*, 17689.
[45] E. L. L. Yeo, N. Ain Azman, J. Chen, Y. Kah, *Langmuir* **2021**, *37*, 4913.

© 2025 The Author(s). Advanced Healthcare Materials published by Wiley-VCH GmbH

21922659, 2025, 15, Downloaded from https://advanced.onlinelibrary.wiley.com/doi/10.1002/adhm.202500846 by Yonsei University Library, Wiley Online Library on [06/04/2026]. See the Terms and Conditions (https://onlinelibrary.wiley.com/terms-and-conditions) on Wiley Online Library for rules of use; OA articles are governed by the applicable Creative Commons License